PROPAGATION MODE ANALYSIS OF UNDERSEA INSULATED SINGLE-WIRE TRANSMISSION LINE WITH OPEN LOSSY BOUNDARY

A PREPRINT

Yuejiu Zhu
School of Precision Instruments and Opto-electronics Engineering, Tianjin University, Tianjin, China
zyj_jy@tju.edu.cn

September 2, 2026

ABSTRACT

Insulated single wires have been employed for undersea wireless power and data transfer systems. The inner conductor, insulating material and seawater form a structure superficially analogous to a coaxial cable, enabling electromagnetic waves to propagate along the single wire over long distances. Underwater units can wirelessly acquire energy or data via couplers placed near the single wire. However, the semi-infinite open boundary of seawater fundamentally alters the electromagnetic propagation regime. Previous works have largely employed quasi-static approximations in the low-frequency limit or antenna-based models at higher frequencies, both assuming a TEM (or quasi-TEM) mode within the dielectric insulation. The TEM assumption underlying both approaches breaks down at electrically significant scales. Starting from Maxwell's equations under the semi-infinite open boundary of seawater, this paper derives the propagation modes of the single-wire transmission line. The analysis reveals that the structure does not support a standard TEM mode, but exclusively the TM_0 mode. The theoretical predictions are validated by full-wave simulations in CST, using a 1 m long insulated wire model with an inner conductor radius of 2.5 mm and a 2 mm thick dielectric insulation layer, in the 1 MHz to 100 MHz range, and are further confirmed by a water tank experiment, in which the measured response contains a single propagating mode whose attenuation agrees with theory. These results provide theoretical support for high-speed underwater wireless communication via single-wire structures.

Keywords undersea single-wire · open boundary transmission line · transmission line mode analysis

1 Introduction

Energy replenishment and information transmission are two major challenges faced by underwater detectors in marine exploration missions. Underwater sensors or other units are typically electrically powered and can readily emit electromagnetic signals. Therefore, electromagnetic-based wireless energy replenishment and data transmission methods have been extensively studied, including capacitive coupling and inductive coupling. However, due to the high electrical conductivity of seawater, wireless electromagnetic energy or electromagnetic signals cannot propagate over long distances in the seawater environment. Consequently, researchers have extended the underwater transmission distance by incorporating cabled connections into the system. Ferrite toroids can be mounted along the cable, or electrode plates can be attached at the cable terminus. Electromagnetic energy can propagate over long distances along the cable, enabling underwater equipment in the vicinity to wirelessly harvest power via either capacitive or inductive coupling[1–4].

Initially, researchers employed a two-conductor transmission line structure[1]. Later, researchers found that at low frequencies, seawater itself is a good conductor and can serve as one of the two conductors. Consequently, single-wire transmission lines submerged in seawater have found widespread application[3, 4]. However, the equivalent electromagnetic parameters of seawater—such as the complex permittivity and loss tangent—are strongly frequency-dependent, determining whether it behaves as a conductor or a dielectric at a given operating frequency. At low frequencies, seawater behaves as a good but lossy conductor. At high frequencies, it gradually transitions toward dielectric behavior. For power transfer applications, researchers typically operate below 1 MHz and model seawater as a lossy conductor[3, 4]. In contrast, for data communication applications, some studies employ higher frequencies such as 433 MHz and approximate seawater as a dielectric medium[2]. The former operates at excessively low frequencies and thus provides inadequate bandwidth for underwater sensor data transmission. The latter incurs prohibitively high attenuation, restricting the signal range to only 2 m. At the more appropriate frequency of 100 MHz, seawater enters the transition region between a good conductor and a dielectric. For a single-wire structure immersed in seawater, the surrounding medium serves as an unbounded, lossy return path. Under these conditions, the propagation mechanism of single-wire transmission in seawater has not been thoroughly investigated.

Wave guidance by single conductors with open boundaries has been studied since the foundational works on surface-wave transmission lines[5–7], which established that a dielectric-coated conductor surrounded by unbounded free space supports a bound, non-radiating surface wave. These classical analyses, however, address structures that differ from the present one in two essential aspects. First, in a classical Goubau line the confinement is provided by the dielectric coating and the field decays losslessly and evanescently in the surrounding air, whereas in the present structure the insulation is electrically thin (2 mm, far below the 3 m wavelength at 100 MHz) and the confinement is instead dominated by the skin effect of the lossy seawater. Second, the classical line is embedded in lossless air, whereas the present line is surrounded by an unbounded, highly lossy seawater region that carries the return conduction current. These differences fundamentally alter the boundary-value problem and call for a dedicated analysis.

In recent years, researchers have also investigated the propagation modes of the same structure. However, their studies were confined to the low-frequency regime below 1 MHz. Moreover, in their theoretical derivation, seawater was assumed to constitute an ideal closed electrical boundary analogous to the outer metallic conductor of a coaxial cable[8, 9]. Consequently, they concluded that this structure primarily supports the TEM mode. Nevertheless, this conclusion is no longer valid at moderately higher frequencies. At these frequencies, the impedance matching results obtained using their method deviate considerably from actual behavior, resulting in significant reflection. This reduces the power delivered from the driving circuit to the cable and limits the transmission distance. Therefore, it is necessary to perform an exact analysis of the propagation modes of the undersea insulated single-wire transmission line without resorting to approximations in the high-frequency band.

The main contributions of this paper are as follows: 1. Starting from Maxwell's equations, the propagation modes of electromagnetic waves in this transmission line are derived by incorporating the constitutive relations and boundary conditions of the undersea insulated single-wire transmission line, which supports exclusively the TM_0 mode. 2. As an illustrative example, a wire comprising a 2.5-mm-radius inner conductor coated with a 2-mm-thick insulation layer is considered. Full-wave simulations are carried out in CST Studio Suite. 3. Experimental validation is conducted in a water tank to verify the theoretical derivation and simulation results.

2 Derivation of Propagation Modes

2.1 Model and Assumptions

The undersea insulated single-wire transmission line typically ranges from tens to hundreds of meters in length. It is generally tethered to a buoy, with the underwater detection unit positioned in proximity to the single-wire cable to acquire power or information via electromagnetic inductive coupling, as shown in Fig. 1.

The cross section of the transmission line is shown in Fig. 2.

The cross-sectional structure comprises three concentric layers from the inside out: the inner conductor, the dielectric insulation layer coated on the conductor, and the surrounding seawater. In practical applications, a single cable, suspended from a buoy and used to deliver power or signals to equipment deployed at depth, typically ranges from 50 m to 300 m in length, and the cable weight must therefore be minimized. By comprehensively considering the hydrodynamic drag from ocean currents, overall weight, and other practical constraints, and in accordance with commonly adopted specifications, we assume an inner conductor radius of 2.5 mm and an insulation thickness of 2 mm for the following derivation. The line is assumed to be infinitely long and uniform along its axis. Given that the seawater domain is significantly larger than the cable radius, it is modeled as a semi-infinite open boundary. The electromagnetic parameters of the three regions are listed in Table 1.

The following notational conventions are adopted throughout the derivation. The time-harmonic factor is taken as $e^{j\omega t}$; the field dependence along the propagation direction (z-axis) is taken as $e^{-j\beta z}$, with the complex propagation constant

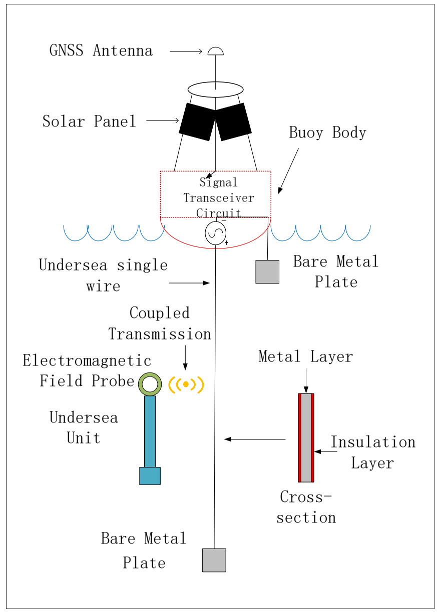

Figure 1: Schematic of the undersea insulated single-wire transmission line system

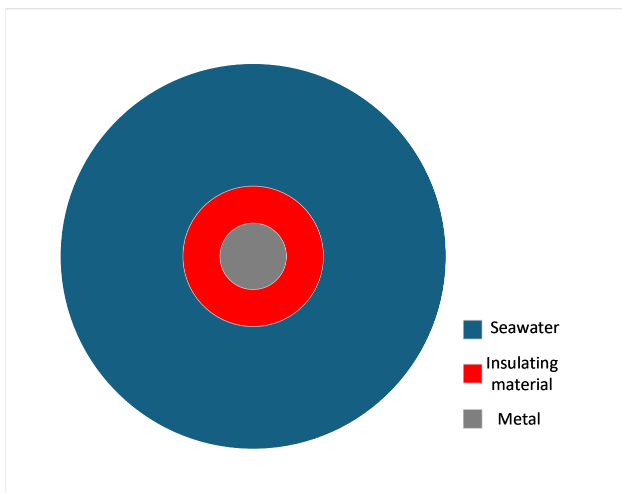

Figure 2: Cross section of the undersea insulated single-wire transmission line.

written as

$$\beta = \beta' - j\alpha, \qquad \alpha > 0 \text{ corresponds to attenuation.} \tag{1}$$

Each region i ($i = 1, 2, 3$ for the inner conductor, the insulation, and the seawater, respectively) is characterized by a complex permittivity

$$\varepsilon_i^* = \varepsilon_0 \varepsilon_{ri} - j\frac{\sigma_i}{\omega}, \qquad k_i^2 = \omega^2 \mu_0 \varepsilon_i^*, \tag{2}$$

where k_i is the complex wavenumber in region i and μ_0 is the permeability of free space, since all three media are non-magnetic. For the copper inner conductor, $\varepsilon_1^* \approx -j\sigma_1/\omega$; for the seawater, $\varepsilon_3^* = \varepsilon_0 \varepsilon_{r3} - j\sigma_3/\omega$; and for the PVC insulation, $\varepsilon_2^* = \varepsilon_0 \varepsilon_{r2}(1 - j \tan \delta)$.

Table 1: Electromagnetic parameters of the three regions.

Region	Parameters
Copper ($\rho < 2.5$ mm)	$\sigma = 5.8 \times 10^7$ S/m
PVC insulation ($2.5 < \rho < 4.5$ mm)	$\varepsilon_r = 3.5$, $\tan\delta = 0.01$
Seawater ($\rho > 4.5$ mm)	$\sigma = 4$ S/m, $\varepsilon_r = 81$

2.2 Field Equations and Boundary Conditions

Within each region the medium is source-free, homogeneous, and isotropic. With the time-harmonic convention $e^{j\omega t}$ and the complex permittivity defined in (2), the time-harmonic Maxwell's equations read

$$\nabla \times \mathbf{E} = -j\omega\mu_0\mathbf{H}, \tag{3a}$$
$$\nabla \times \mathbf{H} = \sigma_i\mathbf{E} + j\omega\varepsilon_i\mathbf{E} = j\omega\varepsilon_i^*\mathbf{E}, \tag{3b}$$
$$\nabla \cdot \mathbf{E} = 0, \qquad \nabla \cdot \mathbf{H} = 0. \tag{3c}$$

Taking the curl of the first equation and substituting the second yields the vector Helmholtz equations

$$\nabla^2\mathbf{E} + k_i^2\mathbf{E} = 0, \qquad \nabla^2\mathbf{H} + k_i^2\mathbf{H} = 0. \tag{4}$$

The structure is translationally invariant along z and rotationally symmetric about the z-axis, so the fields can be expanded in azimuthal harmonics as

$$\mathbf{E}(\rho, \varphi, z) = \mathbf{e}(\rho)\, e^{jn\varphi}e^{-j\beta z}. \tag{5}$$

We take $n = 0$ (axisymmetric fields; the cases $n \geq 1$ are excluded in the next subsection). With $\partial_\varphi = 0$ and $\partial_z \to -j\beta$, the six scalar component equations of (3) split rigorously into two uncoupled groups: the TM group (components E_ρ, E_z, H_φ)

$$j\beta H_\varphi = j\omega\varepsilon_i^* E_\rho, \tag{6a}$$
$$\frac{1}{\rho}\frac{d(\rho H_\varphi)}{d\rho} = j\omega\varepsilon_i^* E_z, \tag{6b}$$
$$-j\beta E_\rho - \frac{dE_z}{d\rho} = -j\omega\mu_0 H_\varphi, \tag{6c}$$

and the TE group (components E_φ, H_ρ, H_z)

$$j\beta E_\varphi = -j\omega\mu_0 H_\rho, \tag{7a}$$
$$\frac{1}{\rho}\frac{d(\rho E_\varphi)}{d\rho} = -j\omega\mu_0 H_z, \tag{7b}$$
$$-j\beta H_\rho - \frac{dH_z}{d\rho} = j\omega\varepsilon_i^* E_\varphi. \tag{7c}$$

There are no coupling terms between the two groups—this is a rigorous consequence of axial symmetry (for $n \geq 1$ the two groups are coupled through the boundary conditions into hybrid EH/HE modes).

Solving the first equation of (6) for $E_\rho = \beta H_\varphi/(\omega\varepsilon_i^*)$ and substituting it into the third equation to eliminate E_ρ, with the transverse wavenumber defined as

$$u_i^2 = k_i^2 - \beta^2, \tag{8}$$

the transverse field components are expressed entirely in terms of the longitudinal component:

$$E_\rho = -\frac{j\beta}{u_i^2}\frac{dE_z}{d\rho}, \qquad H_\varphi = -\frac{j\omega\varepsilon_i^*}{u_i^2}\frac{dE_z}{d\rho}. \tag{9}$$

Substituting (9) back into the second equation of (6), E_z is found to satisfy the zeroth-order Bessel equation

$$\frac{1}{\rho}\frac{d}{d\rho}\left(\rho\frac{dE_z}{d\rho}\right) + u_i^2 E_z = 0. \tag{10}$$

The TE group is completely parallel: H_z satisfies the same equation, and $E_\varphi = \dfrac{j\omega\mu_0}{u_i^2}\dfrac{dH_z}{d\rho}$. Equation (9) shows that, in a structure uniform along z, E_z and H_z constitute two complete sets of degrees of freedom—any field solution can be classified as TM, TE, TEM, or hybrid according to whether E_z and H_z vanish. This is the mathematical basis for classifying modes by their longitudinal field components.

The general solutions of (10) in the three regions are selected according to physical conditions. In what follows, $a = 2.5$ mm denotes the radius of the inner conductor and $b = 4.5$ mm the outer radius of the insulation layer.

Region 1 (copper core): the field must be regular at $\rho = 0$, which excludes Y_0:

$$E_z^{(1)} = D\,\frac{J_0(w\rho)}{J_0(wa)}, \qquad w^2 = k_1^2 - \beta^2 \approx -j\omega\mu_0\sigma_1. \tag{11}$$

An order-of-magnitude estimate gives $|wa| = \sqrt{2}\,a/\delta_1 = 53$ at 1 MHz, rising to 535 at 100 MHz, where δ_1 is the skin depth of copper. Since $|wa| \gg 1$, the field hardly penetrates into the copper core.

Region 2 (PVC insulation): the annular region admits both solutions:

$$E_z^{(2)} = A\,J_0(u\rho) + B\,Y_0(u\rho), \qquad u^2 = k_2^2 - \beta^2. \tag{12}$$

Region 3 (seawater, open boundary): the Hankel function of the second kind is chosen,

$$E_z^{(3)} = C\,H_0^{(2)}(v\rho), \qquad v^2 = k_3^2 - \beta^2, \qquad \operatorname{Im} v < 0. \tag{13}$$

For large arguments, $H_0^{(2)}(v\rho) \sim \sqrt{2/(\pi v\rho)}\,e^{-jv\rho}$, so the branch with $\operatorname{Im} v < 0$ corresponds to radial exponential decay—this is the Sommerfeld radiation condition in a lossy open medium. Zeros of the characteristic equation on this Riemann sheet (the proper sheet) correspond to proper modes, whereas zeros on the sheet with $\operatorname{Im} v > 0$ are leaky waves, which do not belong to the complete orthogonal mode set. Note that, since $|k_3| \gg k_2$, any candidate solution with $\beta \sim k_2$ automatically has $v \approx k_3$ lying on the proper sheet—the field confinement is provided automatically by the skin effect of seawater and does not rely on dielectric total internal reflection (which is impossible here, since $\varepsilon_{r2} = 3.5 < 81$).

At the dielectric interfaces there is no surface current, so the tangential field components E_z and H_φ are continuous; the same continuity holds across the copper interface, where the field inside the copper is represented by the region-1 solution. Imposing these conditions at $\rho = a$ and $\rho = b$ yields four equations:

$$AJ_0(ua) + BY_0(ua) = D, \tag{14a}$$

$$\eta_u\,[AJ_1(ua) + BY_1(ua)] = D\,\eta_w\,\frac{J_1(wa)}{J_0(wa)}, \tag{14b}$$

$$AJ_0(ub) + BY_0(ub) = CH_0^{(2)}(vb), \tag{14c}$$

$$\eta_u\,[AJ_1(ub) + BY_1(ub)] = C\,\eta_v H_1^{(2)}(vb), \tag{14d}$$

where

$$\eta_u \equiv \frac{j\omega\varepsilon_2^*}{u}, \qquad \eta_v \equiv \frac{j\omega\varepsilon_3^*}{v}, \qquad \eta_w \equiv \frac{j\omega\varepsilon_1^*}{w}. \tag{15}$$

Non-trivial solutions of (14) require the coefficient determinant to vanish, which yields the characteristic equation of the mode; this is carried out in the next subsection.

2.3 Solution of the Propagation Modes

Non-trivial solutions of the boundary-condition system (14) exist only if its coefficient determinant vanishes; this condition constitutes the characteristic equation of the transmission line, whose roots give the propagation constant β. Before solving it, the candidate modes can be narrowed down to a single one by the following two arguments.

Step 1: no strict TEM mode exists. Suppose $E_z = H_z = 0$. According to (9), a non-zero transverse field then requires $u_i^2 = 0$, i.e., $\beta = k_i$, and this condition must hold simultaneously in every region where the field does not vanish. The structure, however, spans two distinct media: at 10 MHz, $k_2 = 0.392$ rad/m for the PVC insulation, whereas $k_3 = 12.6 - 12.5j$ rad/m for the seawater, and no complex β can equal both. Hence a strict TEM mode cannot exist. Physically, a TEM mode would require the outer "conductor" to be equipotential, whereas the return current in seawater is a conduction current $\mathbf{J} = \sigma_3\mathbf{E}$ that must be driven by a longitudinal electric field E_z—and $E_z \neq 0$ is precisely the defining feature of a TM, rather than a TEM, mode. The propagating mode of this structure can therefore at most be termed quasi-TEM.

Step 2: all higher-order modes are evanescent in the operating band. For the actual open lossy boundary, the higher-order solutions of the characteristic equation are leaky modes with inherently complex propagation constants, so that no sharp cutoff condition exists; ruling them out rigorously would require searching the complex plane of the multi-valued Hankel functions for every candidate mode family, which is prohibitively complicated. We therefore adopt a simplified model that is most favorable to higher-order modes: replacing the seawater by a perfectly conducting wall, which prohibits any outward radiation and thus confines the field strictly better than the actual lossy open boundary. Under this assumption the cutoff frequencies of the higher-order modes of this structure ($\varepsilon_{r2} = 3.5$) are

$$f_c^{TE_{11}} \approx \frac{c}{\pi(a+b)\sqrt{\varepsilon_{r2}}} = 7.3 \text{ GHz}, \qquad f_c^{TM_{02}} \approx \frac{c}{2(b-a)\sqrt{\varepsilon_{r2}}} = 40.1 \text{ GHz}, \tag{16}$$

two to three orders of magnitude above the operating band. A mode that is below cutoff even under this perfect confinement cannot possibly be guided by the actual open structure, where energy can additionally leak into the surrounding seawater, so the conducting-wall model yields a rigorous lower bound on the cutoff frequencies of the higher-order modes. Here the cutoff-free fundamental TM_0 mode is the first radial solution of the axisymmetric TM family, so the lowest axisymmetric TM mode with a nonzero cutoff is the second radial solution, denoted TM_{02}; under the conducting-wall assumption the structure degenerates into a coaxial line, in which the TEM mode occupies the fundamental slot, and the TM_{02} mode of the present structure therefore plays the role of the TM_{01} higher-order mode of the equivalent coaxial line. Throughout 1–100 MHz, $\beta^2 = k_2^2 - k_c^2 < 0$, where k_c is the cutoff wavenumber, so these modes can only exist as fields evanescent along z, with attenuation constants

$$\alpha_{TE_{11}} \approx 286 \text{ Np/m (decay length 3.5 mm)}, \qquad \alpha_{TM_{02}} \approx 1571 \text{ Np/m (decay length 0.64 mm)}. \tag{17}$$

That is, higher-order modes exist only as near fields around feed points and discontinuities. The attenuation constants in (17) are likewise lower bounds, since radiation leakage into the open seawater would only further increase the decay. Hybrid modes with $n \geq 1$ have cutoff frequencies no lower than the TE_{11} scale, and the same conclusion applies.

Among all candidates, the only mode capable of propagating in the 1–100 MHz range is therefore the cutoff-free member of the $n = 0$ TM family, i.e., the TM_0 mode, whose propagation constant $\beta(\omega)$ is determined by the characteristic equation associated with (14), which we now write out explicitly. Ordering the unknowns as (A, B, C, D), the vanishing of the coefficient determinant of (14) reads

$$\det \begin{bmatrix} J_0(ua) & Y_0(ua) & 0 & -1 \\ \eta_u J_1(ua) & \eta_u Y_1(ua) & 0 & -\eta_w \dfrac{J_1(wa)}{J_0(wa)} \\ J_0(ub) & Y_0(ub) & -H_0^{(2)}(vb) & 0 \\ \eta_u J_1(ub) & \eta_u Y_1(ub) & -\eta_v H_1^{(2)}(vb) & 0 \end{bmatrix} = 0. \tag{18}$$

Eliminating D and C through the first and third rows reduces (18) to a 2×2 transcendental equation in β,

$$\big[\eta_u J_1(ua) - \eta_w r_w J_0(ua)\big]\big[\eta_u Y_1(ub) - \eta_v r_v Y_0(ub)\big] - \big[\eta_u Y_1(ua) - \eta_w r_w Y_0(ua)\big]\big[\eta_u J_1(ub) - \eta_v r_v J_0(ub)\big] = 0, \tag{19}$$

where $r_w = J_1(wa)/J_0(wa)$ and $r_v = H_1^{(2)}(vb)/H_0^{(2)}(vb)$, and u, v, w, η_u, η_v, η_w are functions of β through (8) and (15).

Equation (18) is transcendental in the complex variable β and is solved numerically as follows. All Bessel and Hankel functions are evaluated in 40-digit arbitrary-precision complex arithmetic, and the determinant is evaluated by Gaussian elimination with partial pivoting. The root is refined by a complex Newton iteration on $(\mathrm{Re}\,\beta, \mathrm{Im}\,\beta)$, and convergence is accepted when the determinant magnitude has decreased to below 10^{-9} of its value at the initial guess. Since the TM_0 mode is a Goubau-type surface wave, its root lies in the neighborhood of k_2; the search at the lowest frequency is therefore started from a grid of initial guesses distributed around k_2 in the complex plane, and each subsequent frequency is initialized from the root converged at the previous frequency, so that the same branch of the multi-valued determinant is tracked continuously across the band. The proper Riemann sheet is maintained by taking principal square roots for u, v, w and replacing v by $-v$ whenever $\mathrm{Im}\,v > 0$, which keeps $H_0^{(2)}(v\rho)$ exponentially decaying outward in accordance with (13); among the converged roots, the physical one is selected by $\beta' > 0$ and $\alpha > 0$. The resulting $\beta(\omega)$ over 1–100 MHz is the theoretical curve used for the comparisons in Secs. 3 and 4.

3 Simulation Validation

3.1 3D Modeling and Port Configuration

Full-wave simulations are carried out in CST Studio Suite to independently validate the theoretical model. The simulated structure reproduces that of Sec. 2: a straight insulated wire of length $L = 1$ m ($a = 2.5$ mm, $b = 4.5$ mm) embedded in seawater, with the constitutive parameters listed in Table 1. The wire is driven and terminated by two 50 Ω discrete ports at its ends, each connected between the conductor–insulation interface ($\rho = a$) and the insulation–seawater interface ($\rho = b$), so that the port voltage directly drives the radial electric field of the TM_0 mode across the insulation layer. The seawater domain is truncated at a finite distance with open (radiation) boundary conditions, as illustrated in Fig. 3. The S-parameters are computed over the 1–100 MHz band, and the cross-sectional field distributions at $z = L/2$ are recorded.

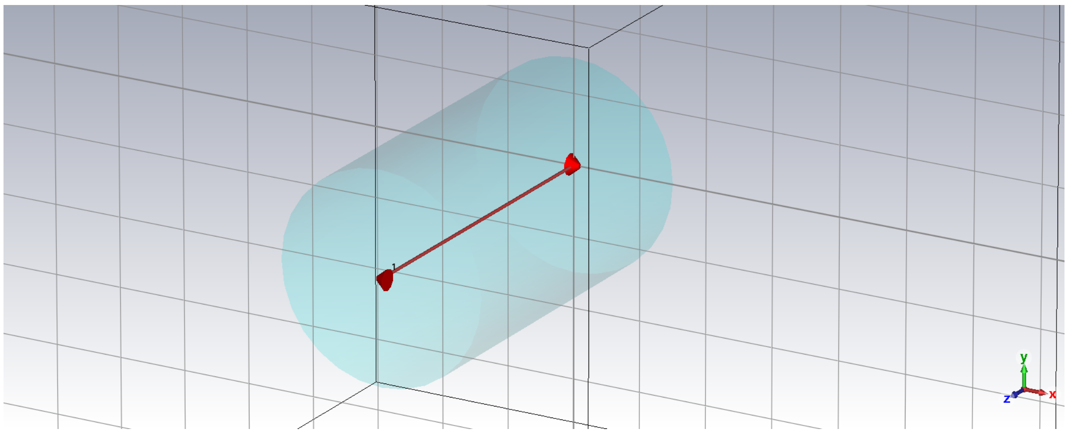

Figure 3: CST simulation model: the 1 m insulated wire embedded in a truncated cylindrical seawater domain, driven and terminated by 50 Ω discrete ports at both ends.

3.2 Mode Identification and Radial Confinement

The mode excited in the simulation is first identified from the cross-sectional fields. Fig. 4 compares the maxima of the field components at 1 MHz and 100 MHz, each normalized to the dominant component of its field. The longitudinal component E_z dominates the electric field, exceeding E_ρ by one to two orders of magnitude and E_φ by about four orders; the magnetic field is essentially azimuthal, with H_z six orders of magnitude below H_φ. In addition, the field is azimuthally symmetric, with $|E_z|$ varying by less than 0.3% along any circle of constant radius. A dominant E_z, a vanishing H_z, and $n = 0$ symmetry jointly identify the simulated mode unambiguously as the TM_0 mode predicted in Sec. 2. The confinement of the mode is illustrated in Fig. 5: at 100 MHz, both $|E_z|$ and $|H_\varphi|$ decay monotonically with the radial distance over nearly three orders of magnitude, until a numerical floor set by the truncated computational domain is reached. The energy is thus bound to the vicinity of the wire rather than radiating into the seawater, confirming the surface-wave character of the TM_0 mode.

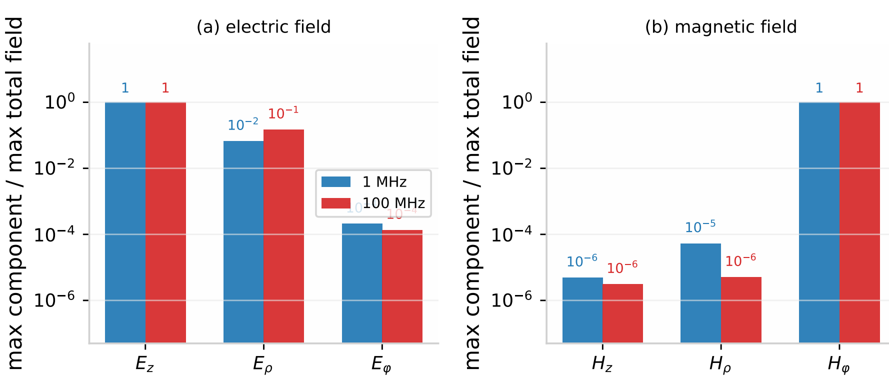

Figure 4: Maxima of the field components on the $z = L/2$ cross-section at 1 MHz and 100 MHz, normalized to the dominant component of each field (E_z and H_φ, respectively).

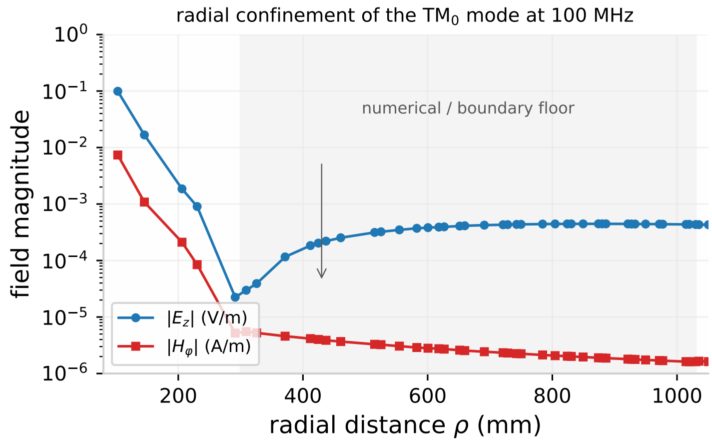

Figure 5: Radial decay of $|E_z|$ and $|H_\varphi|$ in the seawater at 100 MHz. The fields decay monotonically until reaching the numerical floor of the truncated computational domain.

3.3 Propagation Constant Comparison

Quantitative validation is obtained by comparing the propagation constants. The simulated S-parameters of the 1 m wire are shown in Fig. 6: $|S_{11}|$ stays below -14 dB throughout the band, with a minimum of -30.1 dB at 27.7 MHz, so the associated mismatch loss never exceeds 0.31 dB at either port and does not distort the comparison below. The attenuation constant is extracted from the transmission magnitude as $\alpha = -|S_{21}|_{\mathrm{dB}}/(8.686\,L)$, and the phase constant from the unwrapped transmission phase as $\beta' = -\mathrm{unwrap}(\angle S_{21})/L$, after removing the 180° polarity reference phase of the discrete ports. Fig. 7 overlays the simulated values on the theoretical curves obtained by solving the characteristic equation associated with (14) for the same parameters. The theory reproduces both the magnitudes and the trends over the whole band: the phase constant β' spans 0.11–7.6 rad/m and the attenuation constant α spans 0.010–1.29 Np/m, and the two theoretical curves correctly predict the dispersion law of the simulated mode, as evidenced by the parallel slopes in the log-log plot of Fig. 7.

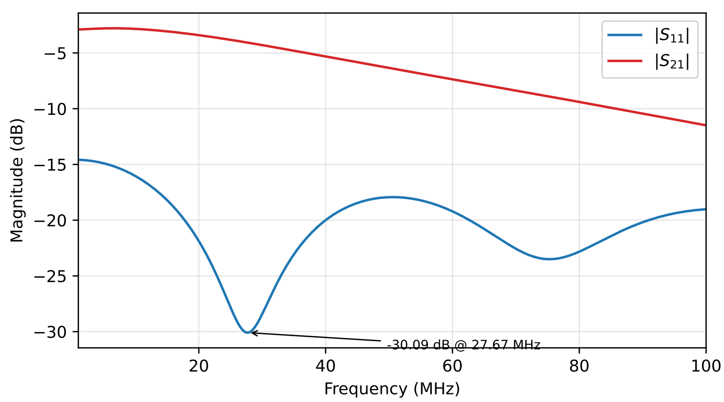

Figure 6: Simulated S-parameters of the 1 m insulated wire over the 1–100 MHz operating band.

Two discrepancies between theory and simulation are visible in Fig. 7, both of which are understood and do not affect the validity of the theoretical model. First, at low frequencies the simulated attenuation saturates at approximately 0.33 Np/m instead of following the theoretical curve down to 0.010 Np/m at 1 MHz. Decomposing $|S_{21}|$ into propagation, mismatch, and residual terms reveals a fixed end-loss that decreases from 2.5 dB at 1 MHz to 0.2 dB at 100 MHz. The physical origin lies in the loose confinement of the mode at low frequencies: the radial decay length of the TM$_0$ mode reaches about 0.25 m at 1 MHz, comparable to the length of the finite wire, so that a fraction of the excited power is not captured by the bound mode and is instead radiated or dissipated at the line ends; as the frequency increases, the mode becomes progressively tighter ($\mathrm{Im}(v)b$ grows from 0.018 to 0.17 across the band), the port coupling becomes

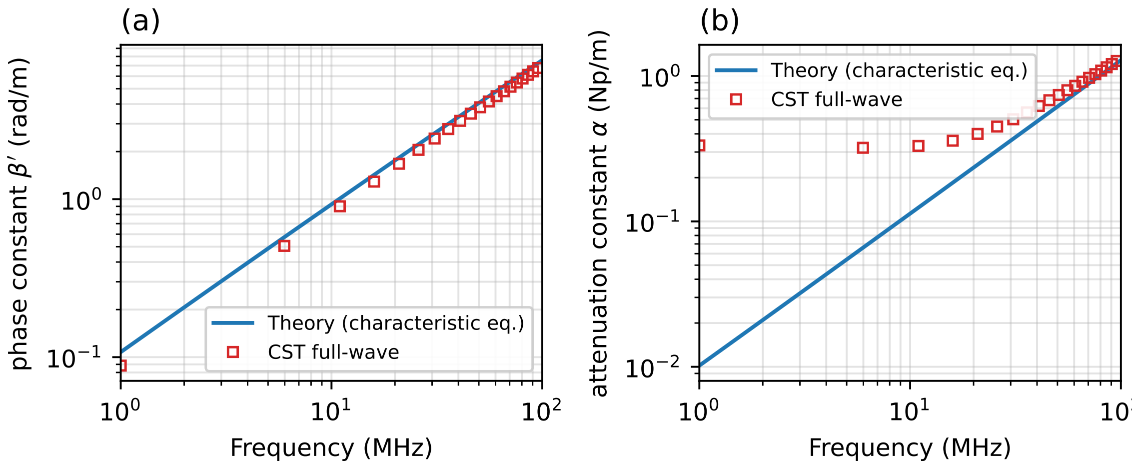

Figure 7: Propagation constants of the TM_0 mode: theoretical curves from the characteristic equation (solid lines) versus values extracted from the CST S-parameters (markers). (a) Phase constant β'; (b) attenuation constant α.

efficient, and the simulated and theoretical attenuation converge, the deviation decreasing from an apparent 97% at 1 MHz to 2.8% at 100 MHz. The low-frequency discrepancy is therefore not an error of the propagation model but a manifestation of the finite line length, and the convergence of the two curves at high frequencies confirms that the theoretical dispersion is correct.

Second, the simulated phase constant sits about 7% below the theoretical value throughout the high-frequency range, forming a constant-fraction offset rather than a decaying one. This systematic deviation is attributed to the differences between the two models rather than to the physics: the theory assumes a semi-infinite seawater region, whereas the simulation truncates the domain at a finite distance, and the discrete ports introduce their own phase reference and local field perturbation. Since β' is sensitive to a few-percent change of the effective permittivity, such model-level differences are sufficient to account for the 7% offset. Importantly, the offset does not grow with frequency, and the identical log-log slopes of the two curves indicate that the dispersion law of the TM_0 mode is correctly captured by the theory.

In summary, the full-wave simulation independently reproduces the identity, confinement, and propagation constants of the TM_0 mode, with discrepancies fully accounted for by the finite line length and the truncated domain of the simulation model. These results validate the theoretical derivation of Sec. 2.

4 Water Tank Experiment

As a further validation, a water tank experiment was carried out. As shown in Fig. 8, an insulated wire of the same cross-section as in Secs. 2 and 3 (copper core of radius $a = 2.5$ mm coated with a 2 mm PVC layer, $b = 4.5$ mm) was laid straight across a 1 m long water tank, so that exactly 1 m of the wire was immersed, and its two ends were connected through coaxial cables to a LiteVNA vector network analyzer with a 50 Ω reference impedance. At each end, the coaxial cable from the analyzer transitions near the water surface to a pair of short alligator-clip leads: one clip is attached to the exposed inner conductor of the insulated wire, while the other is attached to a bare copper terminal inserted directly into the brine, so that the port is effectively applied between the inner conductor and the surrounding water. The tank was filled with a 35‰ saline solution, whose conductivity (≈ 4 S/m) and relative permittivity (≈ 81) reproduce the seawater parameters of Table 1. Both one-port and two-port S-parameter measurements were recorded over 0.1–200 MHz with 101 frequency points; the following analysis uses the 1–100 MHz band, corresponding to 49 effective frequency points between 2.1 and 98.1 MHz ($\Delta f \approx 2$ MHz). To characterize the test fixture (coaxial cables, feed-through connectors, and clip leads), the fixture was additionally measured back-to-back with the wire removed. The measured S-parameter magnitudes are shown in Fig. 9: $|S_{21}|$ rolls off smoothly from about 0 dB at the low-frequency end to -18 dB at 100 MHz, while $|S_{11}|$ rises to about -2 dB. The port mismatch is considerably stronger than in the simulation of Sec. 3, so the time-domain response is expected to contain multiple-reflection echoes in addition to the direct transmission.

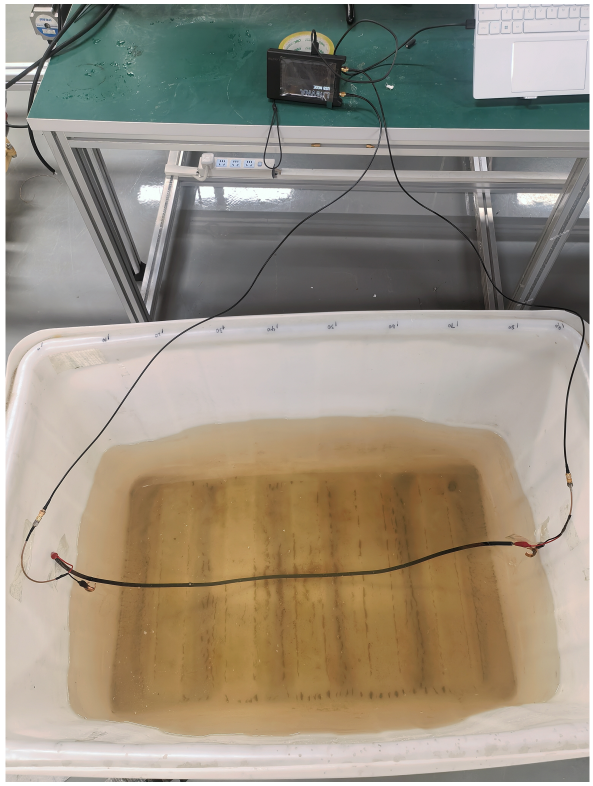

Figure 8: Water tank experiment: the insulated wire is immersed across the 1 m tank filled with 35‰ brine, and connected at both ends through coaxial cables to the LiteVNA vector network analyzer (top).

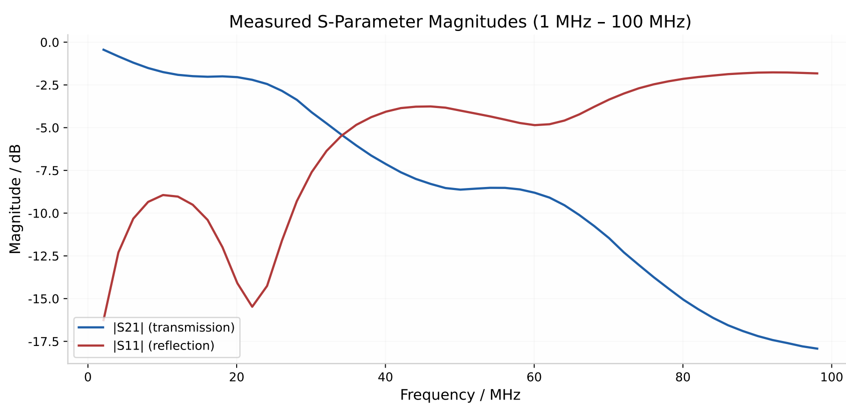

Figure 9: Measured S-parameter magnitudes of the immersed wire over the 1–100 MHz band.

The number of propagating modes is determined from the impulse response of S_{21}. If the line supported N propagating modes, the transmission coefficient would be the superposition

$$S_{21}(\omega) = \sum_{m=1}^{N} A_m(\omega)\, e^{-j\beta_m(\omega)L}, \tag{20}$$

and under weak dispersion the inverse Fourier transform

$$h(\tau) = \mathcal{F}^{-1}\{S_{21}(\omega)\} \approx \sum_{m} A_m\, \delta(\tau - \tau_m) \tag{21}$$

resolves the modes as separate peaks at their respective group delays $\tau_m = (d\beta_m/d\omega)L$, with a time resolution of about $1/\mathrm{BW} \approx 10$ ns for the 96 MHz effective bandwidth. It should be noted that port mismatch also produces peaks, which are located at odd multiples (3τ, 5τ, ...) of the main-peak delay with geometrically decaying amplitudes and must be distinguished from genuine modes. The measured complex S_{21} was windowed by a Kaiser window with shape parameter 6 to suppress sidelobes, zero-padded by a factor of 16, and transformed by a band-pass IFFT; the resulting impulse response, normalized to its main peak, is shown in Fig. 10, and the peak parameters are listed in Table 2. The response exhibits a single dominant peak at 14.7 ns. The only other visible peaks, at 40.2 ns (-17 dB) and 70.2 ns (-36 dB), sit at approximately 3τ and 5τ of the main-peak delay with successively and strongly decaying amplitudes; they are therefore identified as the first and second multiple-reflection echoes rather than additional modes. An independent cross-check based on the phase slope of S_{21} (Fig. 11) yields a group delay whose median over the band is 14.6 ns, coinciding with the main-peak delay, and reveals no second propagating component. The measured line thus supports only one propagating mode in the 1–100 MHz band.

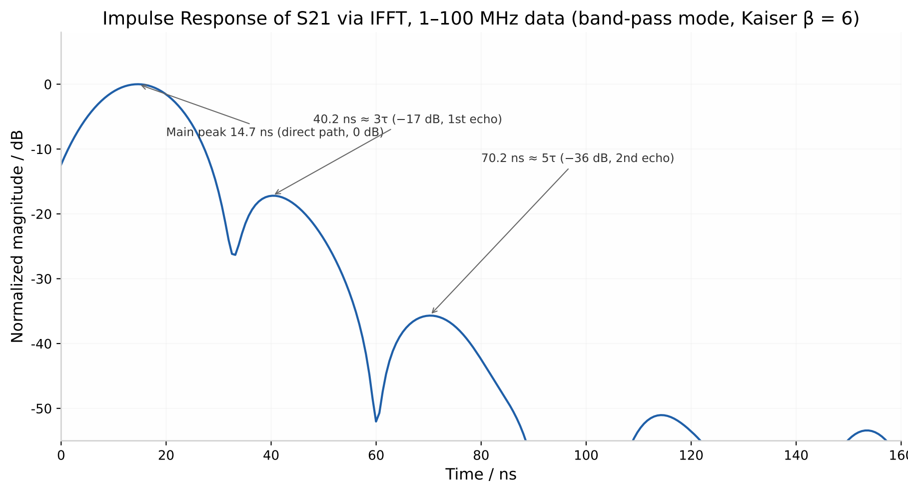

Figure 10: Impulse response of the measured S_{21} obtained by IFFT of the 1–100 MHz data (band-pass mode, Kaiser window with shape parameter 6), normalized to the main peak. The peaks at 40.2 ns and 70.2 ns lie at odd multiples of the main-peak delay and are identified as mismatch echoes.

Table 2: Time-domain peak parameters and identification.

Peak	Delay (ns)	Relative magnitude (dB)	Delay/τ	Identification
Main	14.7	0	1.0	Direct propagation
2	40.2	-17	≈ 3	First echo (3τ)
3	70.2	-36	≈ 5	Second echo (5τ)

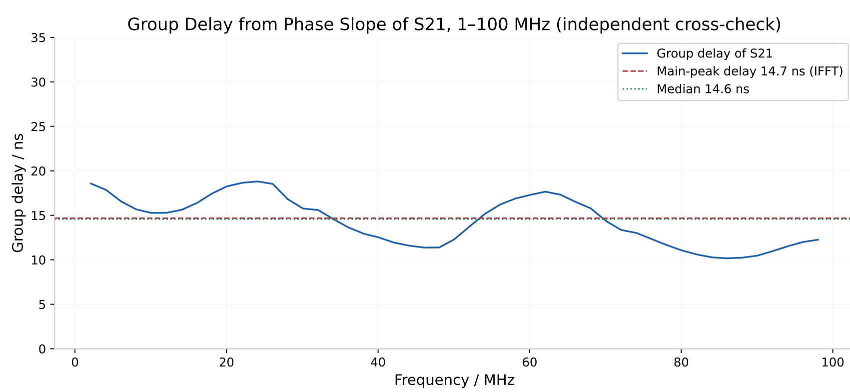

Figure 11: Group delay of S_{21} obtained from the phase slope over 1–100 MHz as an independent cross-check. The median value of 14.6 ns (dotted line) agrees with the main-peak delay of 14.7 ns from the IFFT (dashed line).

That this single propagating mode is indeed the TM_0 mode predicted in Sec. 2 follows from the quantitative consistency between the measured data and the theoretical dispersion. The back-to-back fixture measurement shows that the test fixture itself contributes an insertion loss growing from 0.1 dB at 1 MHz to 5.7 dB at 100 MHz and a group delay of 2.7–7.0 ns; it is therefore the dominant systematic error source and its contribution must be removed before comparing with theory. Subtracting the fixture insertion loss from the measured $|S_{21}|$ yields the net attenuation of the 1 m immersed wire, which agrees with the theoretical attenuation constant of the TM_0 mode to within -21% to $+23\%$ over 3–100 MHz (e.g., 0.615 versus 0.616 Np/m at 50 MHz, and 1.42 versus 1.29 Np/m at 100 MHz), correctly reproducing the growth of the theoretical α from 0.010 Np/m at 1 MHz to 1.29 Np/m at 100 MHz. The net group delay obtained by subtracting the fixture delay has a median of about 9.5 ns for the 1 m line, 20–35% below the theoretical TM_0 group delay per unit length (which decreases from 16.1 ns/m at 1 MHz to 10.9 ns/m at 100 MHz). This residual discrepancy is attributed to the fixture–line mismatch—the fixture return loss degrades to -1.9 dB at 100 MHz, so multiple reflections between the fixture and the line invalidate the simple delay-subtraction de-embedding—and to the coarse 2 MHz frequency step, which makes the phase-slope estimate noisy; the same effect is visible as the large ripples of the net delay across the band. The measured delay nevertheless remains of the order of 10 ns for the 1 m line—well above the 3.3 ns that a free-space wave would accumulate over the same distance—and is consistent in magnitude with the theoretical TM_0 delay. Since the analysis of Sec. 2 excludes any TEM or higher-order mode in this band, and the full-wave simulation of Sec. 3 identifies the same unique mode as TM_0, the experiment completes a three-way validation: theory, simulation, and measurement consistently indicate that the undersea insulated single-wire transmission line supports exclusively the TM_0 mode in the 1–100 MHz band.

5 Conclusion

Starting from Maxwell's equations under the semi-infinite open lossy boundary of seawater, this paper has derived the propagation modes of the undersea insulated single-wire transmission line. The analysis shows that the structure supports no strict TEM mode, and that all higher-order modes are far below cutoff in the operating band; the line therefore supports exclusively the TM_0 mode in the 1–100 MHz range. This conclusion is confirmed by full-wave CST simulations, which reproduce the field structure, confinement, and propagation constants of the TM_0 mode, and by a water tank experiment, in which the measured impulse response contains a single propagating component whose fixture-de-embedded attenuation agrees with theory to within -21% to $+23\%$ over 3–100 MHz.

The significance of this work for subsequent design is threefold. First, the characteristic equation yields the attenuation per unit length for any given frequency and cable structure (inner conductor radius and insulation thickness); combined with the receiver sensitivity, this determines the maximum transmission distance for a given frequency and cable. Second, the field structure and propagation constant of the TM_0 mode provide guidance for the feeding and matching of the single-wire line. Third, the wave impedance in seawater obtained from the mode solution provides guidance for the design of the couplers used by underwater units.

References

[1] Jiayi Xu, Xingfei Li, Ziming Xie, Congcong Fu, and Rong Du. Design and analysis of inductively coupled power transfer system on mooring buoy with double ultracapacitor chargers using indirect control. *IEEE Transactions on Industrial Electronics*, 67(6):4836–4845, 2020. doi:10.1109/TIE.2019.2928249.

[2] Zia M. Loni, Hugo G. Espinosa, and David V. Thiel. Insulated wire fed floating monopole antenna for coastal monitoring. *Radioengineering*, 27(1):127–133, 2018. doi:10.13164/re.2018.0127.

[3] Jiayi Xu, Shui Pang, Shuo Pan, Qingfeng Ma, Xingfei Li, and HongYu Li. Modeling and construction of underwater single wire power transfer system. *IEEE Transactions on Industrial Electronics*, 71(12):16790–16800, 2024. doi:10.1109/TIE.2024.3387081.

[4] Xichen Liu, Chunwei Cai, Shuai Wu, Chenghao Li, Qinyuan Cui, and Xiuyun Ren. Modeling and analysis of undersea capacitive power transfer based on conduction current in seawater. *IEEE Transactions on Power Electronics*, 40(3):4640–4651, 2025. doi:10.1109/TPEL.2024.3498063.

[5] Georg Goubau. Surface waves and their application to transmission lines. *Journal of Applied Physics*, 21(11): 1119–1128, 1950. doi:10.1063/1.1699553.

[6] Georg Goubau. Single-conductor surface-wave transmission lines. *Proceedings of the IRE*, 39(6):619–624, 1951.

[7] Georg Goubau. Open wire lines. *IRE Transactions on Microwave Theory and Techniques*, 4(4):197–200, 1956.

[8] Congyu Yang. Modeling and design of a marine long-distance cabled multi-node inductively coupled communication system. Master's thesis, Tianjin University, 2026. In Chinese.

[9] Luyi Dong. Study on electromagnetic field propagation characteristics of marine single-wire inductively coupled power transfer system. Master's thesis, Tianjin University, 2026. In Chinese.